Estimation of Needleleaf Canopy and Trunk Temperatures and Longwave Contribution to Melting Snow

K. N. MUSSELMAN[a] AND J. W. POMEROY

Centre for Hydrology, University of Saskatchewan, Saskatoon, Saskatchewan, Canada

ABSTRACT

A measurement and modeling campaign evaluated variations in tree temperatures with solar exposure at the edge of a forest clearing and how the resulting longwave radiation contributed to spatial patterns of snowmelt energy surrounding an individual tree. Compared to measurements, both a one-dimensional (1D) energy-balance model and a two-dimensional (2D) radial trunk heat transfer model that simulated trunk surface temperatures and thermal inertia performed well (RMSE and biases better than 1.7° and ±0.4°C). The 2D model that resolved a thin bark layer better simulated daytime temperature spikes. Measurements and models agreed that trunk surfaces returned to ambient air temperature values near sunset. Canopy needle temperatures modeled with a 1D energy-balance approach were within the range of measurements. The radiative transfer model simulated substantial tree-contributed snow surface longwave irradiance to a distance of approximately one-half the tree height, with higher values on the sun-exposed sides of the tree. Trunks had very localized and substantially lower longwave energy influence on snowmelt compared to that of the canopy. The temperature and radiative transfer models provide the spatially detailed information needed to develop scaling relationships for estimating net radiation for snowmelt in sparse and discontinuous forest canopies.

1. Introduction

The melting of seasonal snow cover in forested environments impacts ecosystem productivity (Trujillo et al. 2012), carbon uptake (Monson et al. 2005), and regional water resources (Bales et al. 2006). Forest vegetation structure alters atmospheric fluxes of energy and precipitation in ways that determine subcanopy snow accumulation and ablation processes. Beneath a forest canopy, snow accumulation is largely controlled by canopy interception processes (Pomeroy et al. 1998) and melt energy is primarily in the form of shortwave and longwave radiation (Link and Marks 1999; Pomeroy and Granger 1997; Sicart et al. 2004). Despite the process complexity compared to open environments, many models successfully simulate snow accumulation and melt processes under continuous forest canopies (e.g., Gelfan et al. 2004; Koivusalo and Kokkonen 2002).

However, the fragmentation of forest canopy cover is commonplace in North America as a result of human activity (Riitters et al. 2000) and insect infestation (Coops et al. 2010) compromising forest–snow models predicated on the assumption of canopy-cover homogeneity.

Compared to continuous canopy coverage, snow cover under fragmented forest canopies is exposed to higher and more variable rates of turbulent transfer (Boudreault et al. 2015) and solar irradiance (Musselman et al. 2012; Pomeroy et al. 2008). The lower canopy densities of fragmented forests are generally associated with lower subcanopy longwave irradiance and enhanced shortwave irradiance due to greater sky view (Lundquist et al. 2013); however, the longwave reduction may be partially compensated by additional thermal contribution from sunlit canopy and trunk elements. For example, Pomeroy et al. (2009) and Woo and Giesbrecht (2000) reported high variability of tree temperatures resulting from the heterogeneous heating of sunlit and shaded trunk and canopy elements. In both studies, the largest heating above air temperature values were measured under discontinuous canopy conditions with high solar insolation. While shortwave radiation in discontinuous canopies beneath and around individual trees has been characterized and

modeled (e.g., Ellis et al. 2013; Essery et al. 2008; Musselman et al. 2013, 2015; Pomeroy et al. 2008), less attention has been paid to the spatiotemporal variability of incoming longwave radiation patterns at the snow surface (e.g., Lawler and Link 2011; Seyednasrollah and Kumar 2014). In Alberta, Canada, Bernier and Swanson (1993) reported that longwave radiation from the edges of small canopy gaps enhanced snow sublimation compared to that in larger clearings where the greater distance from canopy edges reduced the forest longwave contribution.

Longwave radiation is also enhanced in proximity to trunks, which when sunlit can exceed air temperature values by 10° to more than 20°C (Pomeroy et al. 2009). The enhanced snowmelt energy alters snow-cover depletion curves and contributes to the formation of snow-free areas that initiate near the trunks and expand outward (Faria et al. 2000; Musselman et al. 2008). Near-trunk accelerated melt has important eco-hydrological and biogeochemical implications. For example, Pomeroy et al. (1999) reported enhanced ion deposition to the winter snow cover nearest the trunks in a boreal forest. In more temperate environments, stemflow and canopy drip processes cause high fluxes of water and solutes within the near-trunk zone [see review by Levia and Frost (2003)]. Accurate simulation of the snowmelt contribution to soil water and nutrient fluxes at the scale of individual trees in fragmented forested environments requires treatment of variable tree temperatures and the resulting energy exchange to the snow surface.

Conifer forest temperatures are commonly modeled in three ways: 1) canopy elements (i.e., needles, trunks, and branches) are assumed to remain in equilibrium with the air temperature, 2) canopy temperatures are simulated with an energy-balance (EB) approach (e.g., Parviainen and Pomeroy 2000), and 3) needle and/or trunk temperatures are specified to exceed the air temperature by a constant empirical value (e.g., Burles and Boon 2011; Seyednasrollah et al. 2013). Recently, Gouttevin et al. (2015) explicitly resolved both canopy and trunk temperatures using an EB approach including heat storage effects. While trunk temperature dynamics had previously been modeled successfully (Derby and Gates 1966; Haverd et al. 2007), Gouttevin et al. (2015) were the first to include EB calculations of trunk temperature and heat storage contributions to the snowpack energy state within a snow model.

To diagnose how solar radiation enhances tree temperatures and then longwave radiation to snow under discontinuous forest canopies, physically realistic tree-scale simulations are required. Tree-scale simulations need to link 1) solar irradiance incident on the canopy and trunk, 2) heat storage in the tree, 3) canopy element temperatures, and 4) longwave exchange between canopy elements and the snow surface. To address these four requirements, we 1) make local radiation measurements representative of that incident on the needles and the vertical trunk; 2) test two trunk temperature modeling approaches: a new radial heat transfer model that explicitly simulates trunk surface temperature and internal heat storage at high computational cost and an efficient trunk surface EB model with parameterized heat storage effects; 3) test the ability of the efficient EB model to simulate needle temperatures; and 4) develop a thermal radiative transfer model to simulate the impact of aspect-dependent needle and trunk temperatures on the spatial patterns of longwave snowmelt energy surrounding an individual tree. The objectives of the study are therefore to 1) develop and compare the abilities of a 2D (radial) trunk heat transfer model and a trunk surface EB model with heat storage treatment to represent measured trunk surface temperatures of an intermittently sunlit tree and 2) simulate the finescale dynamics of canopy- and trunk-contributed longwave radiation to snowpack energetics around a single tree.

2. Methods

a. Study site and measurements

Field data were collected in the Marmot Creek Research Basin, Alberta, Canada (50°57′N, 115°09′W; 1843 m MSL), on the north-northeast edge of a flat 56-m diameter forest clearing (Fig. 1a). Data are presented from a warm, 5-day period (4–8 May 2013) of rapid snowmelt, no precipitation, and nearly complete snow cover.

Meteorological observations were made within 3 m of the clearing edge by a Campbell three-dimensional (3D) sonic anemometer (CSAT3) and a krytpon hygrometer (KH20) positioned on a tripod at a height of 2.4 m (Figs. 1b,c; Table 1). A horizontal Campbell 4-component net radiometer (CNR4) at 2 m height recorded incoming and outgoing shortwave (0.3–2.8 μm) and longwave (4.5–42 μm) radiation. At one meter from the canopy edge, a vertically positioned CNR4 was oriented due south/north at a height of 2 m to record the incoming shortwave and longwave radiation fluxes to and from the forest edge (Fig. 1c). Omega fine-wire (0.075 mm) thermocouples (TCs) were carefully inter-twined with needles and the rough outer bark surface on the southwest side of an Engelmann spruce tree located 2 m from the vertical CNR4. One TC at 1.3-m height was placed on the southwest side of the 0.46-m diameter trunk (Fig. 1d), and four TCs measured needle
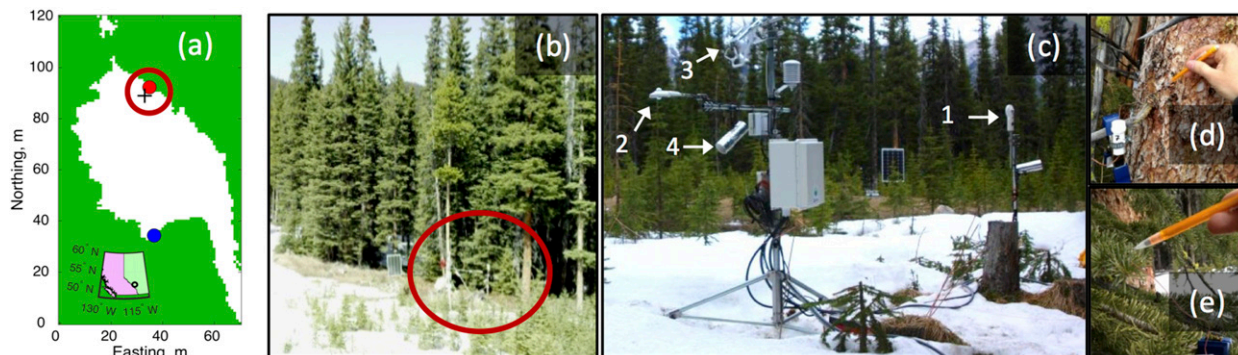
FIG. 1. The clearing study site at the Marmot Creek Research Basin, Alberta, Canada (50°57′N, 115°09′W; 1843 m MSL; see map inset) showing (a) a plan view of the site with the intensively instrumented northeast (sunlit) edge of the clearing circled in red, the meteorological station indicated by the plus sign, and locations of the vertically oriented CNR4 indicated by the red (sunlit edge) and blue (shaded edge) circles; (b) a photo of the northeast clearing edge with instrument locations circled; and (c) the meteorological station design including 1) vertically and 2) horizontally oriented net radiometers, 3) an eddy covariance system, and 4) an infrared thermocouple sensor. Also shown are fine-wire TC sensors placed on (d) a trunk surface and (e) needles. Note that the TCs measured the tree on the right side of the circled region in (b).

temperatures (Fig. 1e) at an average height of 1 m. Note that while the different sides of the trunk were exposed to the direct sunlight for different durations and times of the day, the tree was generally sunlit for much of the day (see Fig. 1). Needle temperatures were measured by TCs positioned on branches over a ~2-m distance ranging from the immediate clearing edge into the tree canopy—this ensured a fairly well-distributed sampling of sun-exposed and shaded needles. A narrow beam infrared radiometer (Exergen infrared thermocouple) measured the radiative temperature of the snow surface (Fig. 1c).

b. Meteorology and tree temperatures

Figure 2 shows the hourly meteorology measured at the forest edge, including the difference between air temperature and temperature of a single trunk and the average of several needles. The average daytime and nighttime air temperatures were 10.9° and 3.4°C, respectively (Table 1); mean wind speeds were low and highest during drainage flows at night; and the skies were clear except for partly cloudy conditions on 7 May (Fig. 2; Table 1). The trunk (bark) surface temperatures deviated from air temperature by as much as 12.2°C with the deviations associated with periods of high solar insolation (Fig. 2). The southwest position of the TC on the trunk at the clearing edge meant that the sensor was shaded until late morning, when trunk surface temperatures substantially increased above the air temperature. On average, the nighttime trunk temperatures deviated very little from the air temperature (Table 1).

TABLE 1. Summary of meteorological observations for the 5-day study period including canopy and trunk deviations from local air temperature.

| Variable	Measured value	Instrument
Mean air temp		
All times	7.2°C	Campbell CSAT3
Day (0800–2000 LST)	10.9°C	Campbell CSAT3
Night (2100–0700 LST)	3.4°C	Campbell CSAT3
Mean relative humidity	50.2%	Campbell KH20
Mean wind speed	$0.69 \, \mathrm{m \, s^{-1}}$	Campbell CSAT3
Cumulative downward SW radiation	$122.0 \, \mathrm{MJ \, m^{-2}}$	Campbell CNR4
Mean downward LW radiation		
All times	$308 \, \mathrm{W \, m^{-2}}$	Campbell CNR4
Day (0800–2000 LST)	$324 \, \mathrm{W \, m^{-2}}$	Campbell CNR4
Night (2100–0700 LST)	$290 \, \mathrm{W \, m^{-2}}$	Campbell CNR4
Deviations from air temp		
Trunk, day (1200–2000 LST)	5.0° (mean); 12.0°C (max)	Omega 0.075-mm TCs
Trunk, night (2100–0700 LST)	0.1°C (mean)	Omega 0.075-mm TCs
Canopy, day (1200–2000 LST)	3.0° (mean); 5.5°C (max)	Omega 0.075-mm TCs
Canopy, night (2100–0700 LST)	−0.4°C (mean)	Omega 0.075-mm TCs
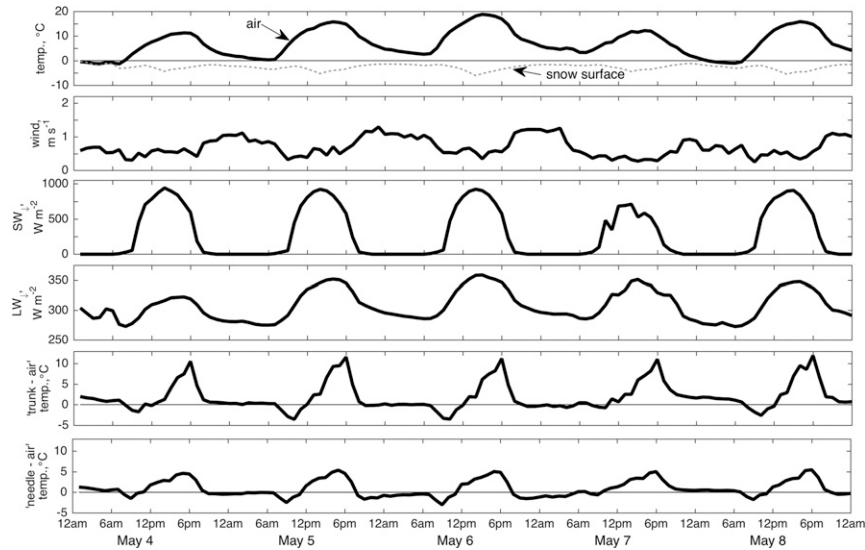
FIG. 2. Hourly average meteorological variables: 2-m air temperature and wind speed, snow surface temperature, horizontal shortwave and longwave radiation, and the surface temperature deviation from air temperature of a spruce trunk and needles during the 5-day study period.

Needle temperature deviation from air temperature was less than that of the trunks and daytime deviations coincided with periods of solar insolation (Fig. 2). On average, needles were 3.3°C warmer than the air temperature during the day with spikes as high as 5.5°C, presumably due to solar heating. At night, average needle temperatures were 0.4°C cooler than air temperatures, possibly due to longwave radiative cooling. The observations indicate substantial energetic differences among sun-exposed and shaded needles and trunks that may be resolved in an EB modeling approach that explicitly considers the

spatiotemporal variability in shortwave and longwave irradiance.

Shortwave and longwave radiation measured on 6 May 2013 by the net radiometers oriented horizontally (i.e., upward facing) and vertically (i.e., north and south facing) are shown in Fig. 3 and summarized in Table 2. For this warm, cloud-free day, the upward-facing shortwave sensor measured greater cumulative incoming shortwave irradiance ($25.94\,\mathrm{MJ\,m^{-2}}$) than the sensors either facing north toward the forest ($2.44\,\mathrm{MJ\,m^{-2}}$) or south into the clearing ($18.07\,\mathrm{MJ\,m^{-2}}$; Table 2). The mean longwave irradiance was greater for lateral fluxes
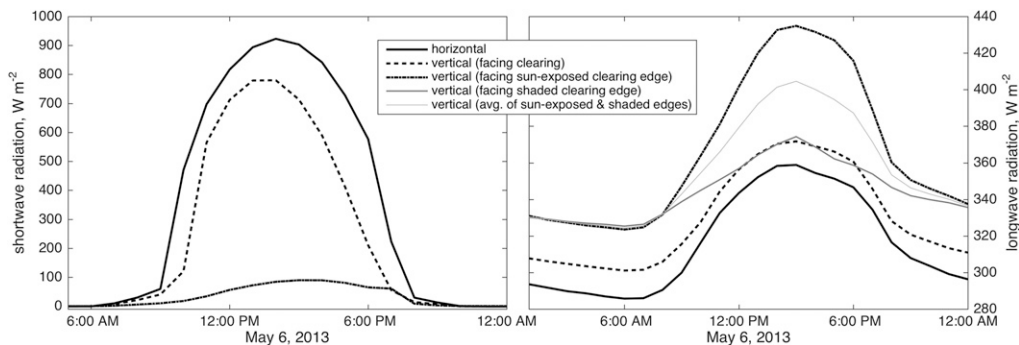

FIG. 3. Hourly average (left) shortwave and (right) longwave radiation measured on 6 May 2013 on the north edge of the forest clearing by horizontal and vertically oriented sensors. The thin gray line on the right is the estimated longwave irradiance on the north side of a tree (located on the sun-exposed clearing edge but facing into the forest) calculated as the average of measured values from the vertical sensor (facing the sun-exposed clearing edge) and an identical sensor facing the forest but on the shaded south clearing edge (facing the shaded clearing edge; see legend). Time on the *x* axis is local standard time.

TABLE 2. Summary of shortwave and longwave radiation observations for 6 May 2013.

	Vertical fluxes (facing upward)	Horizontal fluxes[a] (facing north toward forest)	Horizontal fluxes[b] (facing south toward clearing)
Shortwave (cumulative; MJ m^{-2})	25.94	2.44	18.07
Longwave (mean; W m^{-2})	316	367 (356)[c]	330

[a] Upright radiometer measuring horizontal fluxes from the forest toward the clearing.
[b] Upright radiometer measuring horizontal fluxes from the clearing toward the forest.
[c] Estimated longwave incident on the north side of a trunk, computed as the mean of measured horizontal longwave fluxes (sensor facing forest) shown in Fig. 3 and the horizontal (sensor facing clearing) longwave measurements made on the shaded (south) edge of the clearing.

from the forest edge (367 W m^{-2}) and from the clearing (330 W m^{-2}) than the incoming flux measured by the upward-facing sensor (316 W m^{-2}), which had more sky view than the lateral-facing sensors.

c. Distributing radiation on a vertical trunk

Figure 3 compares the incoming shortwave and longwave radiation measured by the upward-facing sensor on 6 May 2013 to the lateral radiation measured by the north- and south-facing sensors. While estimates of shortwave and longwave irradiance on north- and south-facing vertical surfaces were available from measurements, it was necessary to interpolate these observations to other trunk orientations (i.e., north, northeast, . . . , west, northwest). The interpolation of shortwave radiation required separate treatment of the direct and diffuse components. Shortwave radiation measured by the upright south-facing sensors was partitioned into the direct and diffuse components using the all-sky model presented in Allen et al. (2006) and modified to account for the solar incidence angle relative to a south-facing vertical plane (Duffie and Beckman 1980; Garnier and Ohmura 1968). Estimates of incoming diffuse and direct beam shortwave irradiance on the south face were used to estimate the total (i.e., global) irradiance on the other faces. The north-facing sensor was always shaded from direct sunlight and therefore was assumed to measure only diffuse radiation. Diffuse radiation was assumed to be equal on the east and west sides of the trunks and was estimated as the average of the (calculated) south-face and (measured) north-face diffuse values. Diffuse irradiance values were linearly interpolated from the nearest two cardinal directions to the four intermediate azimuthal faces.

To estimate the direct beam irradiance on all faces of a trunk, a trigonometric multiplicative correction factor was used as an approximation to adjust the partitioned value computed from measurements available only on the south-facing side:

$$\xi(t, \overline{\delta}_n) = \frac{1 + \cos[\vartheta(t) - \overline{\delta}_n]}{2}, \quad (1)$$

where the correction factor $\xi(t, \overline{\delta}_n)$ describes the fraction (from 0 to 1) of the shortwave direct beam component projected on a vertical curved surface oriented at mean azimuth $\overline{\delta}_n$ of arc segment n relative to the solar azimuth ϑ at time t. Note that ϑ is defined as 0 to the north and increases in a clockwise direction. The circular cross section of a trunk was divided into eight arc segments, each with an average $\overline{\delta}_n$ direction. A ξ value of 1 indicates full sun projected on the curved surface while a 0 value indicates that the curved segment is self shaded. The measured incoming shortwave irradiance on the south- and north-facing sensors were assumed to represent the trunk-incident values and were not corrected (see Fig. 3).

Longwave irradiance to the eight trunk faces was estimated from values measured by the vertically oriented sensors using the same averaging described for diffuse shortwave irradiance, except for one difference. The north-facing vertical longwave sensor was aimed toward the forest edge that received substantial daytime solar heating. Thus, the longwave irradiance measured by this sensor was positively biased compared to what the shaded, north side of the tree would receive from the south sides of neighboring trees farther into the forest. The longwave radiation incident on the north side of the trunk at the sun-exposed clearing edge was estimated as the average of measurements from the north-facing vertical sensor and another south-facing vertical sensor (oriented toward the forest) located on the shaded edge of the clearing (see Fig. 3, Table 2).

3. Models

a. Trunk heat transfer PDE model

The heat transfer equation for a 2D, horizontal circular cross section of a tree trunk is

$$\rho c_p \frac{\partial T}{\partial t} - \nabla \cdot (k \nabla T) = Q, \quad (2)$$

where ρ is the mass (bark or trunk) density (kg m^{-3}), c_p is the specific heat capacity (J kg^{-1} K^{-1}), k is the

coefficient of trunk heat conduction ($W\,m^{-1}\,K^{-1}$), and $T = T(x, y, t)$ is the temperature (K) at a specified node in horizontal space (m) and time t (s). The term Q is an internal heat source/sink term that can be used to account for latent heat exchange, that is, freezing and thawing; however, it was assumed equal to $0\,W\,m^{-2}$ for this springtime study during which air temperatures were generally $>0°C$. Vertical heat transfer was assumed to be negligible. An outer bark layer surrounding the inner trunk was represented as a thin (0.007 m, measured) disk surrounding the larger trunk.

Neumann-type boundary conditions were set at the bark–air interface:

$$\mathbf{n} \cdot (k\nabla T_i) + q T_i = R_{net}, \tag{3}$$

where the vector $\mathbf{n}$ specifies the direction normal to the trunk, T_i is the temperature at the boundary, q is the heat transfer coefficient ($W\,m^{-2}\,K^{-1}$), and R_{net} is the net radiation ($W\,m^{-2}$) at the bark–air boundary. The qT_i term in Eq. (3) represents turbulent exchange processes occurring at the boundary. The parabolic partial differential equations (PDE) were solved using the finite element method. The 2D domain was discretized into a triangulated mesh composed of 837 nodes and 1512 elements for the 0.46-m diameter trunk; a higher node density was specified near the bark layer. Nodes located on the outer boundaries were divided into eight azimuthal segments (i.e., north, northeast, east, etc.) and each segment, composed of approximately 10–15 nodes, had a unique boundary condition. The problem is nonlinear because R_{net} is proportional to the fourth power of surface temperature, which is not known a priori. The R_{net} at time t was prescribed for the ($n = 8$) azimuthal trunk segments as

$$R_{net}(n, t) = SW_{in}(n, t)(1 - \alpha) + \varepsilon[LW_{in}(n, t)$$
$$- \sigma T_{tr}(n^*, t')^4], \tag{4}$$

where α is the trunk albedo, ε is the trunk emissivity, σ is the Stefan–Boltzmann constant $5.67 \times 10^{-8}\,W\,m^{-2}\,K^{-1}$, $SW_{in}(n, t)$ and $LW_{in}(n, t)$ are the incoming shortwave and longwave radiation, respectively, and $T_{tr}(n^*, t')$ is the (simulated) trunk surface temperature at model nodes included in azimuthal segment n at model iteration t' of time step t. The sensible heat transfer H ($W\,m^{-2}$) between the bark surface and the air is defined as $H = hA(T_{tr} - T_a)$, where A is the exposed surface area of the trunk per unit area of ground, h is the convection coefficient, and T_a is the air temperature. The heat transfer coefficient, formulated in the form required by Eq. (3), is

$$q(n, t) = hA\left[1 - \frac{T_a(t)}{T_{tr}(n^*, t')}\right]. \tag{5}$$

Convection of sensible heat between the trunk surface and surrounding air has not been extensively studied but is important for surface temperature calculations. Convection can be estimated for an upright cylinder of specified radius with radially invariant air temperature and wind speed, where h for an upright cylinder is the sum of forced-convection h_{forced} and free-convection h_{free} terms (Haverd et al. 2007; Monteith and Unsworth 2013). The Nusselt number Nu_{forced} was used to estimate the degree of turbulent transfer due to forced (wind driven) convection as a function of the Reynolds number as in Haverd et al. (2007). The forced-convection coefficient was calculated as

$$h_{forced} = \frac{\rho_a c_{p,a} D_h Nu_{forced}}{2 r_{1.3\,m}}, \tag{6}$$

where D_h is the molecular diffusivity for heat in air ($20.2 \times 10^{-6}\,m^2\,s^{-1}$ at 10°C; Denny 1993); ρ_a is the air density ($kg\,m^{-3}$) computed from measured values of temperature, atmospheric pressure, and relative humidity; $c_{p,a}$ is the specific heat of air ($1006\,J\,kg^{-1}\,K^{-1}$); $r_{1.3\,m}$ is the trunk radius at a trunk height of 1.3 m; and Nu is the Nusselt number. For free (temperature driven) convection, the Nusselt number was estimated following Haverd et al. (2007) from the Grashof number Gr, which is a function of the temperature gradient

$$Gr = 1.58 \times 10^8 L^3 (T_{tr} - T_a). \tag{7}$$

The free-convection coefficient was calculated as

$$h_{free} = \rho_a c_{p,a} D_h Nu_{free}/L, \tag{8}$$

where the length term L is assumed to be half of the total trunk height and $Nu_{free} = 0.11 Gr^{0.33}$ ($10^4 < Gr < 10^9$) or $Nu_{free} = 0.58 Gr^{0.25}$ ($10^9 \le Gr < 10^{12}$) (Haverd et al. 2007).

The heat transfer equation was solved in a transient analysis performed for 3600 one-second time steps. The model was initialized with radially constant air temperatures and produced hourly temperature estimates for all bark (surface) and trunk (internal) nodes.

b. Trunk surface EB model

The trunk surface temperature can be calculated by solving the energy-balance equation:

$$R_{net} = H + LE + S, \tag{9}$$

where H is the sensible heat flux, LE is the latent heat flux (assumed to be negligible), and S is the heat flux

storage (Gouttevin et al. 2015). Net radiation at the trunk surface was calculated using Eq. (4). The trunk surface temperature T_{tr} to the fourth power makes the R_{net} term, and thus Eq. (9), nonlinear. The net radiation can be linearized around the trunk surface temperature at the current (and previous) time step as

$$R_{net}(t) = c_1(t) + c_2 T_{tr}(t), \qquad (10)$$

where $c_1(t) = SW_{net}(t) + LW_{in}(t) + 3\sigma\varepsilon T_{tr}(t-1)^4$ and $c_2 = -4\sigma\varepsilon T_{tr}(t-1)^3$, where $SW_{net}(t)$ is the net shortwave radiation computed as $SW_{in}(t)(1-\alpha)$. Net radiation was estimated iteratively using the value from the previous computation step as the initial value. See Braud (2000) for the full derivation of Eq. (10).

The heat flux storage ($W\,m^{-2}$) at time t can be estimated as in Gouttevin et al. (2015):

$$S(t) = \beta \frac{T_{tr}(t) - T_{tr}(t-1)}{\Delta t}, \qquad (11)$$

where β is the trunk heat mass ($J\,K^{-1}\,m^{-2}$), Δt is the model time step (s) and the numerator contains the temperature difference (K) between current and previous time steps. The trunk heat mass is considered constant and defined as

$$\beta = V_{tr}B\rho_{tr}c_p, \qquad (12)$$

where V_{tr} is the trunk volume below the canopy base height h_{cb} estimated as the volume of a truncated cone with bottom and top radii $r_{tr,2}$ and $r_{tr,1}$, respectively: $V_{tr} = 1/3\pi h_{cb}(r_{tr,2}^2 + r_{tr,1}^2 + r_{tr,2}r_{tr,1})$, and B is the trunk basal area specified as $0.004\,m^2\,m^{-2}$ from measurements by Hall et al. (2003). The trunk surface EB model converged in fewer than four time step iterations and provided hourly surface temperature estimates for eight azimuthal trunk segments.

c. Canopy EB model

The trunk EB model was modified to estimate the temperature of a tree canopy T_c (K) composed of needles exposed to the same radiative fluxes from the eight azimuthal directions (i.e., north, northwest, ..., west, northwest) described previously. Modifications to the trunk EB model included a needle shortwave absorption parameter, sensible heat flux calculations within a resistance scheme, and definition of needle heat mass following Gouttevin et al. (2015). Latent heat fluxes were neglected for this snow-covered early spring period. The shortwave canopy extinction parameter was found as $1 - e^{-kLAI}$, where k is the (unitless) needle extinction coefficient specified as 0.8 and LAI is the effective leaf area index specified from measurements as

$2.95\,m^2\,m^{-2}$ (Musselman et al. 2015). The canopy sensible heat flux H_c was estimated as

$$H_c = \frac{\rho_a c_{p,a}(T_c - T_{a,above})}{r_a}, \qquad (13)$$

where r_a is the aerodynamic resistance to heat transfer and $T_{a,above}$ is the above-canopy (15 m) air temperature. Assuming neutral conditions and similar roughness lengths for momentum and heat, r_a is simply estimated as

$$r_a = \frac{1}{k^2 u_{15m}}\left[\ln\left(\frac{Z-d}{z_0}\right)\right]^2, \qquad (14)$$

where k is the von Kármán constant, u_{15m} is the above-canopy wind speed, Z is the 15-m reference height, d is the displacement height (m) specified as $0.63h_c$, and z_0 is the canopy roughness length specified as 2 m.

d. Longwave radiative transfer model

Modeling the longwave radiative transfer from a tree element A_i to a surface area, that is, grid cell, representing the snow surface S_j requires, in addition to the temperature and emissivity of the two surfaces, knowledge of the geometric configuration factor or view factor $F_{A_i \to S_j}$ (Howell et al. 2010). The view factor describes the fraction of energy emitted and reflected by tree surface A_i that is received by surface S_j. Calculation of $F_{A_i \to S_j}$ requires double integration over both surfaces separated by distance R:

$$F_{A_i \to S_j} = \frac{1}{\pi A_i}\int_{A_i}\int_{S_j}\frac{\cos\theta_i\cos\theta_j}{R^2}dA_i\,dS_j, \qquad (15)$$

where θ is the angle between the normal of the surface and the line connecting the surfaces. Analytical solutions of Eq. (15), typically obtained by contour integration, are available in the literature for a range of geometries (e.g., Howell et al. 2010). Figure 4 shows the assumed geometry of a tree represented by a cone (canopy crown), truncated cone (trunk), and partially obstructed disk (canopy base; Fig. 4). Holchendler and Laverty (1974) provide closed-form solutions to estimate F from a differential horizontal surface element dS to 1) a truncated cone and 2) the underside of an annular disk bisected and partially obstructed by a vertical cone. The original configurations and calculations were used to determine radiative exchange within an engine cavity but are equally applicable to tree–snow radiative exchange. The view factor calculations are described in the appendix. The radial symmetry of the single-tree model and small scale ($L = 0.1\,m$) of the defined grid cells
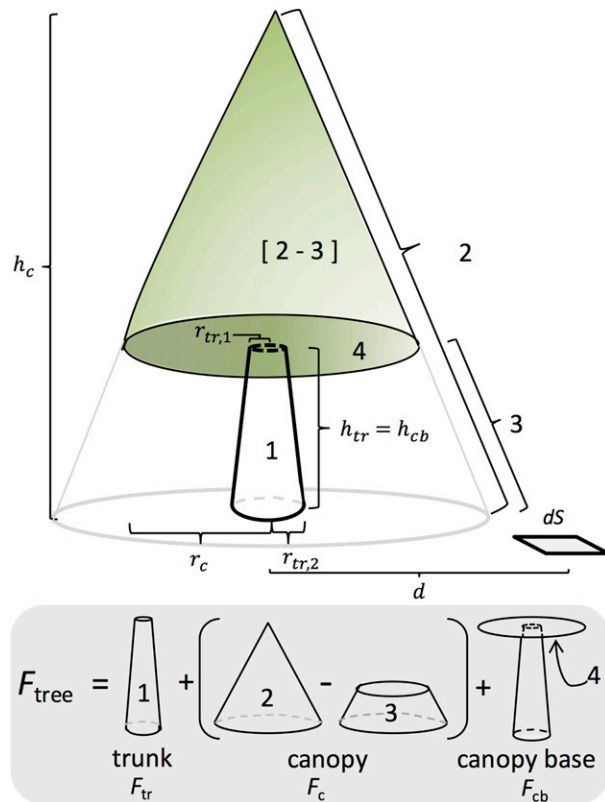
FIG. 4. Geometric configurations representative of a conifer tree trunk (truncated cone; 1), canopy (difference between a two truncated cones; 2 and 3), canopy base (disk partially obscured by trunk cone; 4), and a neighboring horizontal differential element (dS) representative of the snow surface located a distance $\dot{x}$ from the central axis. The configuration was used to estimate the geometric view factor of the trunk and canopy shapes from the perspective of the snow surface needed to model the longwave irradiance using estimates of snow, trunk, and canopy temperatures.

permits the assumption that $F_{dS_j \rightarrow A_i}$ (see appendix) varies only in the radial direction. The reciprocity relation (Howell et al. 2010) was used to estimate $F_{A_i \rightarrow S_j}$, defined as the fraction of radiation emitted and reflected from canopy element surface A_i that is received by the snow surface grid cell S_j. To account for the variability of temperature with surface aspect, Eq. (1) was used to compute the $N = 8$ aspect-weighted average of simulated tree element temperatures when viewed from a particular gridcell location (x, y):

$$\overline{T}_{x,y}(t) = \frac{\sum_{i=1}^{N} T(t,n)\xi(t,n)}{\sum_{i=1}^{N} \xi(t,n)}. \quad (16)$$

In this way, $\overline{T}_{x,y}(t)$ represents a time-variant spatial field of effective tree radiative temperature, as viewed from

the snow surface, which varies smoothly over the snow surface with aspect relative to the tree. In other words, Eq. (16) permits the nonisothermal emission of long-wave radiation from the tree canopy and trunk to the snow surface.

The longwave radiation energy emitted per unit time from a geometric surface with effective temperature $\overline{\tau}$ and emissivity ε is the sum of radiation emitted and reflected by that surface, known as the exitance J:

$$J = \varepsilon\sigma T^4 + (1 - \varepsilon)\text{LW}_{\text{in}}. \quad (17)$$

For canopy elements, J was calculated as a spatial, time-variant array using $\overline{T}$ in place of T and aspect-weighted averages of incoming vertical longwave radiation computed in the same way as the effective temperatures [Eq. (16)]. The snow surface exitance was calculated as a time-variant vector using the measured snow surface temperature and horizontal downward longwave radiation in Eq. (17). The longwave radiation per unit area contributed from surface i received by snow surface j is

$$\dot{Q}_{i \rightarrow j} = \frac{A_i F_{i \rightarrow j} J_i - A_j F_{j \rightarrow i} J_j}{A_j}. \quad (18)$$

From the reciprocity relation, Eq. (18) simplifies to

$$\dot{Q}_{i \rightarrow j} = \frac{A_i}{A_j} F_{i \rightarrow j}(J_i - J_j) \quad (19)$$

and can be converted to a time-integrated energy quantity (MJ m^{-2}). Finally, the longwave irradiance from tree elements to the snow surface is expressed in terms of the potential snowmelt energy equivalent (mm) assuming an isothermal and saturated snowpack:

$$M_{i \rightarrow j} = \frac{\dot{Q}_{i \rightarrow j}}{\rho_w \lambda_f} 1000, \quad (20)$$

where ρ_w is the density of water (1000 kg m^{-3}), λ_f is the latent heat of freezing, and the 1000 multiplier converts meters to millimeters of snow water equivalent.

e. Model implementation

Hourly meteorological observations were used to estimate the trunk and needle temperatures on eight aspects (i.e., north, northeast, ..., west, northwest) of a 13-m tall Engelmann spruce located on the north-northeast edge of the forest clearing (Fig. 1). The canopy (needle) albedo and emissivity values were specified as 0.2 and 0.96, respectively. The trunk albedo and emissivity values were specified as 0.09 and 0.96, respectively. Trunk properties were specified as

trunk density $\rho_{tr} = 900 \, \text{kg m}^{-3}$ (Gouttevin et al. 2015) and trunk heat conduction $k_{tr} = 0.32 \, \text{W m}^{-1} \, \text{K}^{-1}$ (Haverd et al. 2007). Spruce bark was assumed to have a lower water content than the trunk wood but higher than reported for processed bark (Kain et al. 2013); bark properties were thus specified as $\rho_b = 500 \, \text{kg m}^{-3}$ and $k_b = 0.15 \, \text{W m}^{-1} \, \text{K}^{-1}$. The tree had a measured trunk diameter of 0.46 m at 1.3 m height and a 2-m canopy radius extending 2.23 m from the trunk center. The canopy base height and the trunk length term [Eq. (6)] were specified as 20% the total tree height, or 2.6 m, that is, that visible from the perspective of the surrounding snow surface (see Fig. 1). The models produced hourly estimates of needle/trunk temperatures for the 5-day study period.

Thermal snowmelt energy was estimated as the flux from a single (model) tree (see Fig. 4) to an idealized snow-covered model domain. The modeled tree structure was defined from measurements. Thus, the longwave radiative transfer model simulates how this tree at the edge of the forest clearing (see Figs. 1, 4) would radiate thermal energy to an idealized snow surface. The synthetic experiment is a first step toward quantifying a realistic thermal irradiance field surrounding a forest clearing—a combined result of complex signatures from the sky, neighboring trees, occlusion, multiple reflections, and variable surface (snow and/or bare ground) temperatures. A 30 m × 30 m snow-covered domain gridded at 0.1 m spacing was centered on the model tree. The surrounding snow surface was assumed to have an emissivity of 0.985 and a time varying but spatially invariant radiative temperature as measured by the downward-looking infrared TC.

4. Results

a. Temperature model evaluation

The PDE model simulations of hourly trunk temperatures at all nodes shown in Fig. 5 are illustrated for a single cloud-free day (6 May 2013; Fig. 6). The bark surface experienced the highest temperatures, which had a simulated range of 15.8°C depending on the trunk aspect and time of day. The line plot in Fig. 6 (top) shows the simulated bark surface temperatures for all trunk aspects (shading) and select aspects (line colors) compared to air temperature values (dashed line). Surface temperatures on the north side of the trunk were closest to air temperature values (Fig. 6, top), with the mid-afternoon daily maximum coinciding with the timing of the daily maximum air temperature (see Fig. 2). Surface temperatures on the eastern aspects peaked earliest in the day before falling back to north aspect temperatures by 1800 local standard time (LST). South aspect
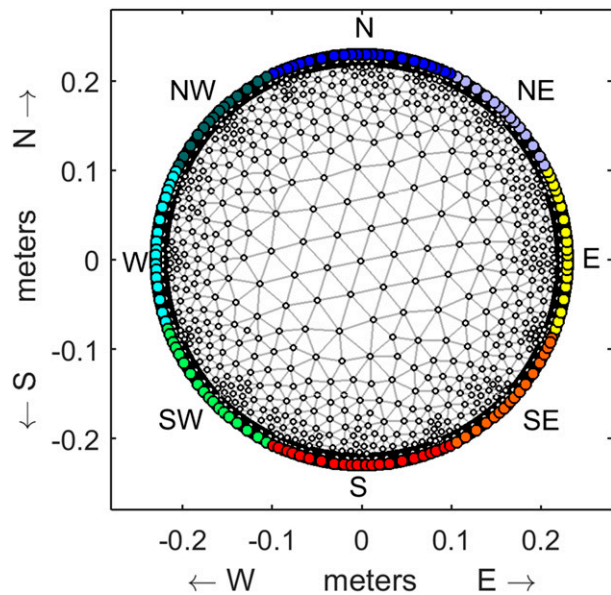

FIG. 5. Trunk temperature PDE model structure for a 0.46-m diameter trunk. Locations of internal nodes (677; empty circles) and boundary nodes (160; colored circles) are indicated. The boundary node colors correspond to the eight azimuthal segments (labeled), each of which specified unique boundary conditions in the model. The 0.007-m bark layer is represented as the black outer edge.

temperatures peaked at the highest temperatures (36.3°C) of all aspects an hour after solar noon. The western aspect temperatures peaked later in the day at temperatures 6°C higher than the eastern aspects. All trunk surface temperatures returned to air temperature values by 1900 LST (local sunset), approximately 2 h after the tree became shaded by the surrounding forest and a tall peak to the west (see Fig. 3).

Figure 6 shows the diurnal progression of surface and internal trunk temperatures simulated by the PDE model as a series of 2D cross sections. The eastern sides of the trunk were heated earliest in the day (1000 LST) transitioning to the southeast (1300 LST) with a gradual wave of warmer temperatures slowly progressing inward from the bark surface. This internal residual warmth from solar heating remained on the east side of the trunk (1300 and 1600 LST) while the south and southwest surfaces were heating in response to direct solar irradiance. After sunset, surface cooling processes caused the warmest simulated temperatures to remain between the surface and the core. The center of the trunk experienced the lowest temperature gradients. Internal heat storage continued through the night despite the trunk surfaces cooling to air temperature values.

The PDE (surface and internal temperatures) and EB (surface temperatures with parameterized heat storage)
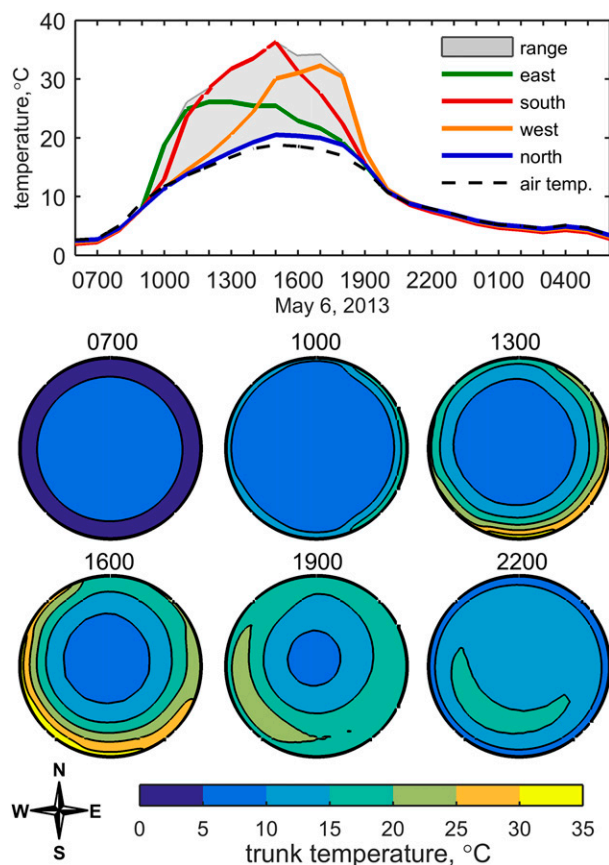
FIG. 6. (top) Simulated trunk surface temperatures by the PDE model on the sun-exposed (i.e., north) edge of the clearing at hourly time steps on 6 May 2013. The gray shading illustrates the range of simulated values on all eight sides (east, northeast, north, etc.) of the trunk. The colored lines indicate the hourly surface temperatures (computed as the average of aspect-specific surface nodes shown in Fig. 5) simulated on four select sides (i.e., east, south, west, and north). The dashed line indicates the measured hourly air temperature. (bottom) Trunk cross sections showing the 2D distribution of internal trunk temperatures (color scheme) simulated by the PDE model for six select hours on 6 May. Note that the contour line values correspond to the tick marks on the color bar.

models were evaluated on their ability to simulate the trunk surface temperatures measured by the fine-wire TC intertwined in the bark on the southwest side of the trunk. Figure 7 (top) compares the two model estimates to hourly average thermocouple and air temperature measurements for the 5-day study period. Generally, the trunk surface temperature estimates from the two models were highly similar and close to measured values. The RMSE values were on average lower for the PDE model (1.38°C) than for the EB model (1.79°C). During the day, the PDE model (1.44°C) outperformed the EB model (2.19°C) while the EB model had slightly lower nighttime RMSE values (Table 3). Average

model biases were better than ±0.5°C and were generally negative, particularly for the EB model. Both models had negative nighttime biases near −0.5°C. The PDE model that incorporated a thin bark layer was slightly better at predicting daytime temperature spikes than the EB model (Fig. 7, top; Table 3).

Needle temperature estimates by the canopy EB model were generally less accurate than either of the trunk surface temperature models. Simulated needle temperatures were on average positively biased (0.65°C; Table 4) but captured the measured daytime needle temperature exceedance of air temperature (Fig. 7, bottom). Daytime RSME values for the canopy EB model were generally in the same range as those from the trunk surface EB model; however, the canopy EB model had higher nighttime RMSE values. The canopy EB model failed to capture the measured nighttime cooling of needles below the reference air temperature, resulting in a positive nighttime bias (0.63°C; Fig. 7, bottom). Overall, needle and trunk surface temperature biases smaller than ±1.0°C are considered quite good given the complexity of the thermal environment and challenges of measuring tree surface temperatures with TCs.

b. Longwave radiative transfer from a single tree to a snow surface

Figure 8 shows maps of F computed for a flat snow surface of the three geometric shapes representing a single tree. In general, the F values decline nonlinearly with distance from an object with high values dependent on both proximity and relative orientation. The maximum F of the canopy crown (0.22) is smaller than that of the canopy base (0.31) or trunk (0.29), but has a larger spatial extent due to the greater prominence of the crown on the horizon at distances beyond the canopy extent. The crown is not visible from the snow surface directly beneath it. The canopy base has the highest maximum F value because of the close proximity to the snow surface and relative orientation, with the highest values occurring directly beneath the crown and at a slight distance from the view-occluding trunk. The trunk occupies a small fraction of the total view except for the snow surface within approximately 1 m of the trunk. Combined, the view factor (i.e., F) values computed for the snow surface around the tree composed of the three shapes had two areas of local maxima: 0.52 about 20 cm from the trunk decreasing to 0.21 at a distance equal to the canopy radius, and a second maxima of 0.40 just beyond the crown edge as a result of higher canopy crown visibility. The tree view factor is low at greater distances from the center of the trunk: 0.15 at 4 m, 0.05 at 7 m, and 0.01 at 14.5 m. The F values suggest that a single
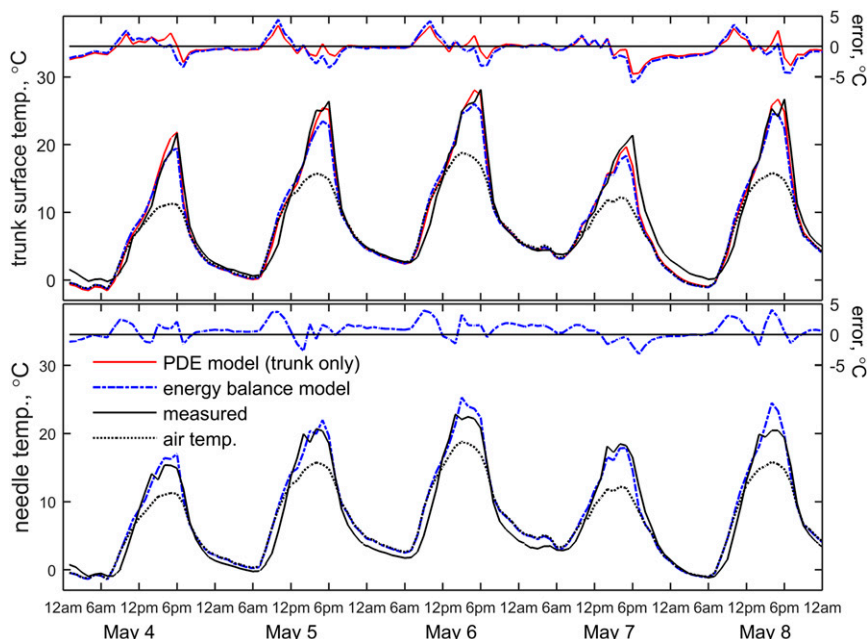
FIG. 7. (top) The left y axis shows hourly trunk surface temperatures on the southwest side of the trunk estimated from the PDE model (red solid line) and EB model (blue dashed line) compared to hourly average thermocouple (black solid line) and air temperature (black dashed line) measurements. The right y axis shows trunk surface temperature model error reported as modeled minus measured. (bottom) Comparison of needle temperatures on the southwest side of the tree estimated from the EB model to measurements. The shading indicates the modeled temperature range for all simulated sides of the tree.

tree will have relatively localized longwave radiative influence on the snow surface energy balance.

Despite trunk surface temperatures greatly exceeding needle temperatures (Fig. 7), the longwave radiative transfer model simulated far greater melt energy contributed by the combined canopy (crown + base) than by the trunk (see Fig. 9). Averaged over the warm 5-day study period, the canopy provided the longwave energy snowmelt equivalent of >20 mm day^{-1} to distances of 1.25 m from the trunk, 7 mm day^{-1} at 3 m, and 1 mm day^{-1} at 7 m. By comparison, the trunk contributed only 4.1 mm day^{-1} closest to the trunk on the south side and 3.3 mm day^{-1} on the north side. At 1 m from the trunk, the longwave melt equivalent was 0.6 mm day^{-1} (Fig. 9).

The longwave radiation contributed from the tree (canopy + trunk) to the snow surface was higher on the sun-exposed south side of the tree than on the shaded north side. Figure 10 illustrates this thermal anisotropy with a plot of the potential melt differences computed as the difference between the southern and northern halves of the model domain; note that only the southern half is displayed. The differences are positive, which indicates that higher longwave melt equivalent on the south aspect is due to solar heating of the canopy and

trunk. As much as 1.8 mm day^{-1} of longwave energy snowmelt equivalent can be attributed to solar aspect differences with most of this energy focused beneath the canopy and nearest the trunk (Fig. 10).

Figure 11 compares the relative importance of resolving canopy and trunk temperatures compared to an assumption that the elements are at air temperature. The canopy temperature equals air temperature assumption results in melt errors of higher magnitude (2–3 mm day^{-1}) and greater spatial extent than assuming that trunks are at air temperature (Fig. 11). For example, at 1 m from the south side of the trunk, the error from

TABLE 3. Trunk PDE and EB model error metrics RMSE and bias evaluated against thermocouple measurements.

	PDE (°C)	EB (°C)
RMSE		
All times	1.38	1.79
Day (0800–2000 LST)	1.44	2.19
Night (2100–0700 LST)	0.71	0.63
Bias		
All times	−0.27	−0.46
Day (0800–2000 LST)	0.11	−0.11
Night (2100–0700 LST)	−0.51	−0.50

TABLE 4. Needle EB model error metrics RMSE and bias evaluated against thermocouple measurements.

	EB (°C)
RMSE	
All times	1.53
Day (0800–2000 LST)	1.97
Night (2100–0700 LST)	0.89
Bias	
All times	0.65
Day (0800–2000 LST)	0.90
Night (2100–0700 LST)	0.63

assuming that the trunk is at the air temperature was only 0.2 mm day^{-1} compared to a 3 mm day^{-1} error at the same location from assuming that the canopy radiates at the air temperature. The results support the findings that individual trunks have very localized longwave energy influence on snow, thus minimizing the large-scale hydrological importance of resolving trunk temperatures.

5. Discussion

a. Trunk and needle temperatures

The measurement and modeling of needle and trunk temperatures and the subsequent estimation of long-wave contribution from a single tree to the surrounding snow surface builds upon previous literature to improve the understanding of forest–snow energy exchange. In an early modeling study, Derby and Gates (1966) used a finite-difference method that accounted for radiation and convection processes to estimate the subdiurnal temperature variations of a trunk cross section. The authors noted a nearly instantaneous response of trunk surface temperatures to changes in meteorological conditions due to a balance of insolation and convective
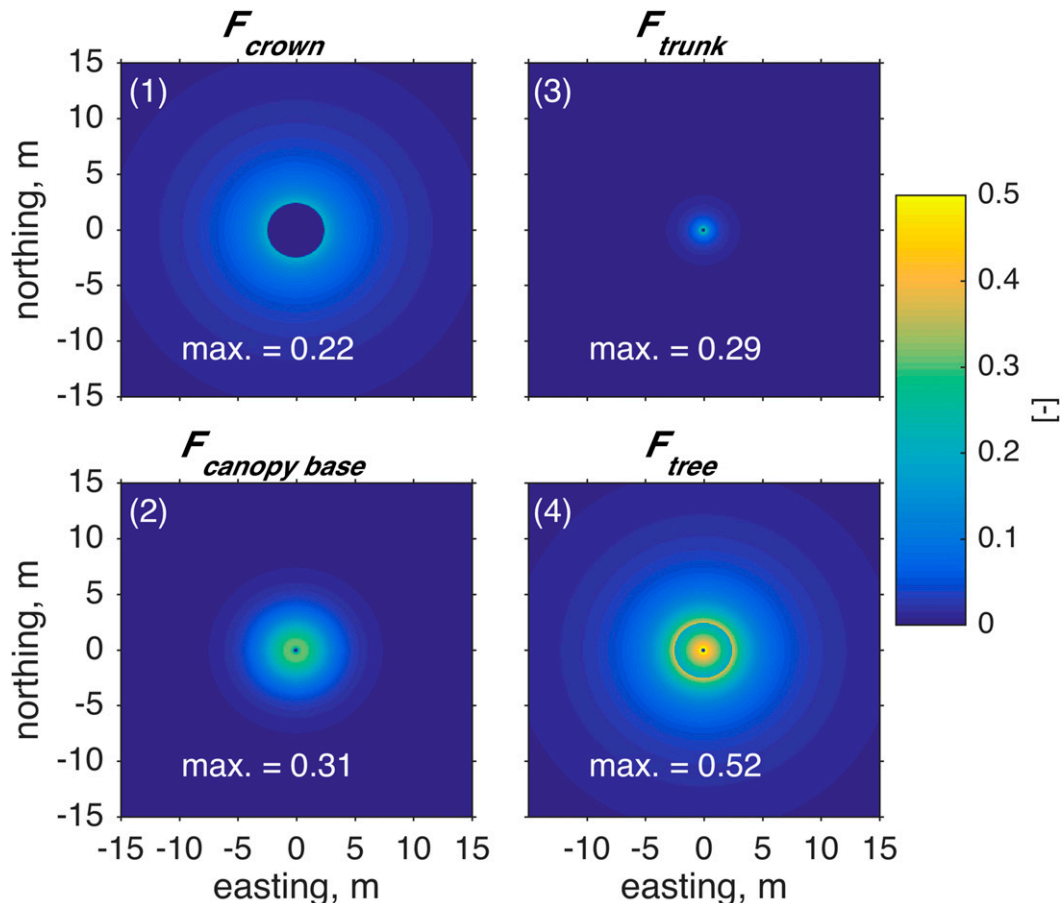

FIG. 8. View factors for a gridded horizontal snow surface (30 m × 30 m; 0.1-m grid spacing) of a single 13-m-tall tree centered at (0,0) composed of three geometric objects: 1) a 2-m radius conical crown offset from the ground by 6.5 m, 2) a 2-m radius disk representing the underside of the canopy partially occluded by the trunk, and 3) a 0.46-m diameter trunk represented as a truncated cone. The fourth panel shows *F* for a full tree represented as the combined crown, canopy base, and trunk geometric shapes. The max *F* value within each image is indicated.
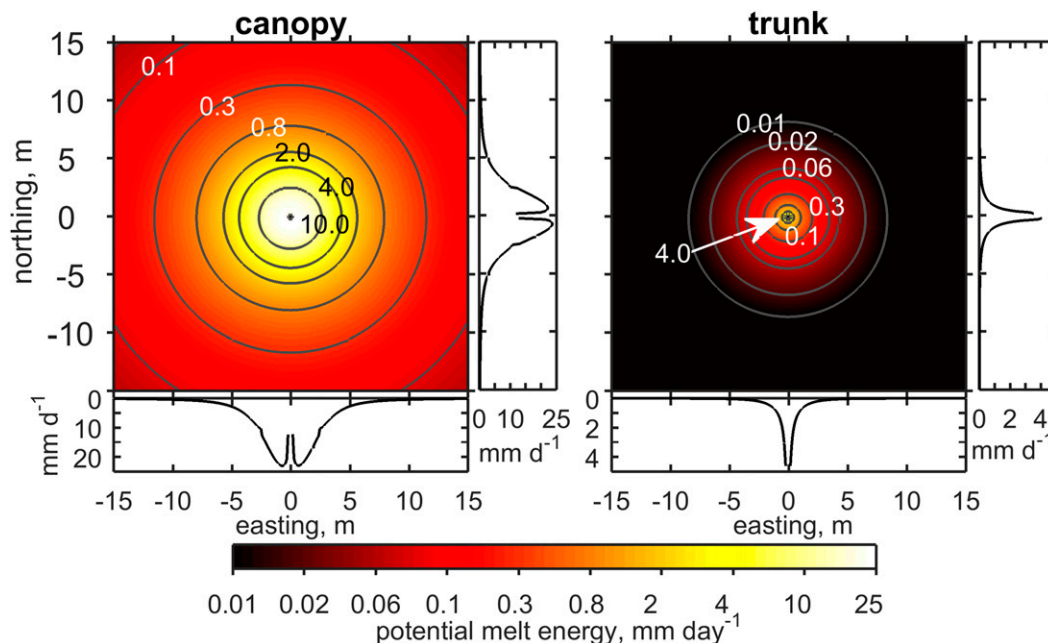
FIG. 9. Potential daily average snowmelt energy from longwave radiation at the snow surface ($30\,\text{m} \times 30\,\text{m}$ domain) simulated over the 5-day study period contributed from the (left) canopy and (right) trunk of a centrally located single tree on the north-northeast edge of the forest clearing. The color scheme is scaled logarithmically and contour intervals correspond to the color bar tick marks. The linearly scaled side panels illustrate the central cross section of melt energy in the east–west (horizontal plots) and north–south (vertical plots) directions.

losses, while internal temperatures exhibited a substantial time delay and dampening affect due to radial heat diffusion. For the purpose of estimating surface longwave exchange, knowledge of the trunk surface or radiative ''skin'' temperature is critical. Pomeroy et al. (2009) found strong agreement between the trunk surface temperatures measured by fine-wire TCs inserted by hyperdermic needle into the bark exterior and a narrow-beam infrared TC aimed at the bark surface. As in the current study, the trunk surface temperature measurements reported by Pomeroy et al. (2009) did not exhibit the clear temporal delay relative to air temperature that has been reported by studies that use TCs placed at trunk depths of 1–2 cm (e.g., Gouttevin et al. 2015; Haverd et al. 2007). The latter studies have used this measured internal temperature phase shift and dampening of the trunk temperature wave relative to air temperatures to validate the inclusion of thermal inertia in trunk temperature simulations. While the PDE model presented here verifies these internal trunk temperature dynamics, the results support a nearly instantaneous response of trunk skin surface temperatures to changes in meteorological conditions (Derby and Gates 1966). In particular, the PDE model predicted daytime trunk temperature gradients in excess of $4°\text{C}\,\text{cm}^{-1}$ in the outer 2 cm of the trunk, where measurements are commonly

made. The results suggest that care should be taken to ensure that trunk temperature measurements are representative of the intended thermal environment.

By resolving the surface and internal energy exchange processes, including heat storage, the PDE model served as a benchmark estimation of the trunk surface temperature. Compared to measurements, the PDE model
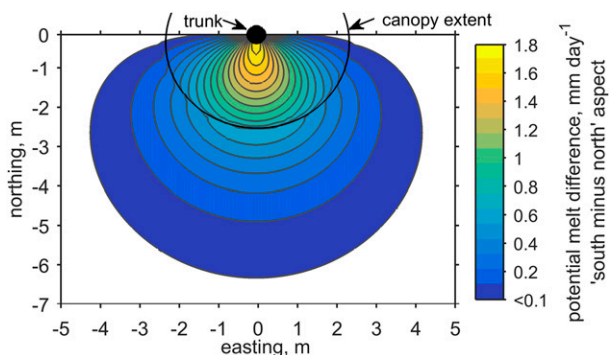

FIG. 10. Solar aspect–derived potential melt differences between the south and north aspects of a tree (combined canopy and trunk) with southern sun exposure during the 5-day study period in early May. The positions of the modeled tree trunk and canopy extent are shown and only the southern half of the domain is plotted as south minus north.
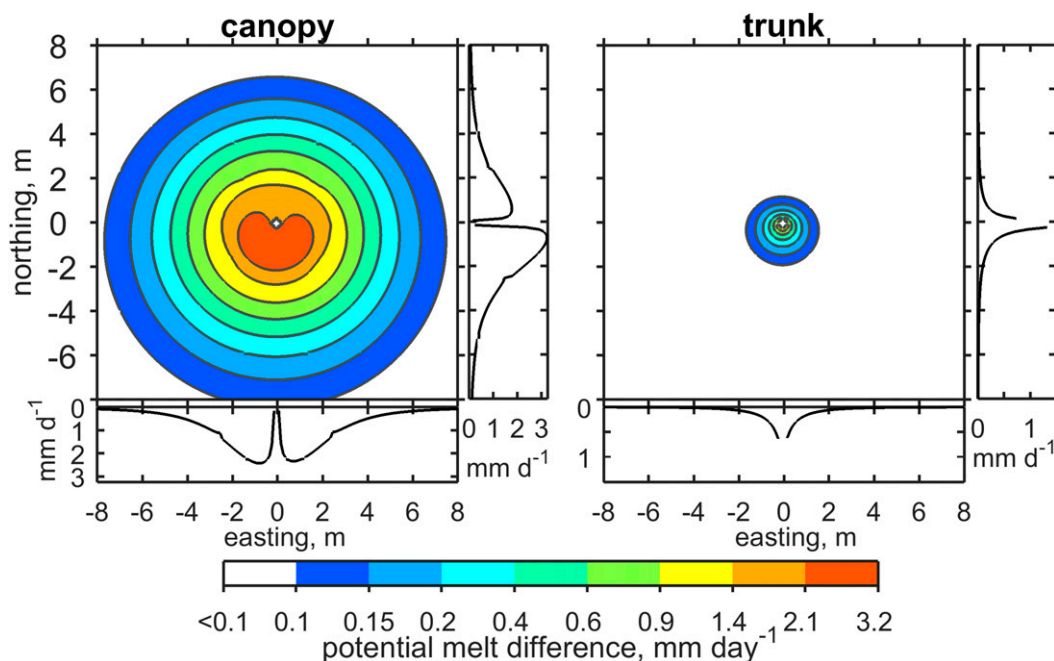
FIG. 11. As in Fig. 9, but for potential melt error (difference) from assuming that the (left) canopy and (right) trunk elements are at air temperature compared to results using the simulated temperatures. Results are averaged over the 5-day study period in early May. The color scheme is scaled logarithmically and contour intervals correspond to the numerical intervals on the color bar.

only slightly outperformed the trunk EB model (Fig. 7, Table 3). The improved daytime performance of the PDE model is attributed to the inclusion of a thin bark layer with lower specified values of bulk density and thermal conductivity than the interior trunk wood, consistent with a lower water content of the rough outer bark surface. Importantly, the strong agreement among the simulated and measured trunk surface temperatures illustrates a high level of skill despite stark differences in model complexity. For example, the 1D trunk surface EB model ran the 120 hourly time steps for eight trunk faces in <0.01 s on a modern laptop computer, while the 2D PDE model that solved the heat transfer equation at 837 nodes required nearly 20 min. Future development of the PDE model to estimate the latent heat exchange during trunk freeze–thaw cycles could help to inform future parameterizations of heat storage processes in simple trunk surface temperature EB models.

The simulation of how trunk surface and needle temperatures vary by aspect and time of day is a critical advancement of previous work. For example, very high–resolution model studies of spatial snowmelt patterns around a single tree (Woo and Giesbrecht 2000) and a forest stand (Giesbrecht and Woo 2000) have treated trunk and canopy temperatures, and hence vegetation longwave exitance, as isotropic. The solar exposure of canopy and trunk elements will vary from full sun to

shade, resulting in a range of tree element temperatures, which helps to define the thermal environment. The explicit EB solution forced with radiation terms determined from vertical sensors has provided unprecedented detail of the subdiurnal evolution of needle and trunk temperatures explicitly resolved on all sides of a tree. The high range of solar exposure of the south-facing clearing edge provided end-member temperature estimates defining the daytime temperature ranges of trunks (15.8°C) and needles (8.0°C) representative of a heterogeneous forest environment (see shading in Fig. 7). By comparison, the calculated nighttime temperature ranges of trunk surfaces and needles were small at <0.8°C. Offline attempts to reduce the positive nighttime needle temperature bias (0.63°C) with an atmospheric stability correction (e.g., Högström 1996) were unsuccessful and may have been challenged by strong nocturnal drainage winds (see wind speed plots in Fig. 2). Note that the model did not resolve the vertical temperature profile of the canopy and trunk; this assumption was deemed appropriate for this sun-exposed clearing edge with strong diurnal mixing of the air space, but may be less robust in smaller gaps that can act as a cold air sink with lower subcanopy shortwave irradiance (Webster et al. 2016). Future work with ray tracing (e.g., Musselman et al. 2013, 2015) and lidar-derived sky view metrics (Moeser et al. 2015) could resolve nonuniform vertical gradients in

air temperature and radiative forcing by solving the EB equations at specified canopy heights.

Subdiurnal forest temperature ranges simulated by the computationally efficient trunk and needle EB models could be used to inform statistical distributions of the forest temperature; an issue relevant to scaling of data between study plot measurements and land surface models (Woo and Giesbrecht 2000). Furthermore, improved representation of canopy element temperatures may subsequently improve land surface model estimates of canopy air space temperatures—a known source of uncertainty in climate models (Vidale et al. 2003). For example, Haughton et al. (2016) show that land surface model errors in the canopy air temperature can cause errors in sensible and latent heat fluxes that are noncompensatory and result in error propagation. Additionally, the simulation of canopy element heating and subsequent localized longwave exchange to the soil/snow surface within finescale models will permit the inclusion of feedback between forest density and net surface radiation, a critical model requirement to simulate the water and energy-balance impacts of forest fragmentation. The improved physical realism of such models is required to test and inform forest management decisions.

b. Longwave contribution from a single tree to melting snow

The higher simulated melt energy contributed from the canopy than from the trunk suggests that the view factor, rather than the relative temperature difference between a tree element and the snow surface, exerts first-order control on the thermal energy exchange (see Fig. 9). For example, despite daytime needle temperatures 1°–6.5°C cooler than that of trunks (Table 1), the canopy contributed more than 33 times the trunk-contributed longwave snowmelt equivalent at a distance of 1 m from the trunk (Fig. 9) as a result of the very small (~0.05) trunk view factor even at that short distance (Fig. 8). The highly localized trunk view factors shown in Fig. 8 correspond to the localized longwave energy contribution from trunks to the surrounding snow cover (Fig. 9, right). The results are consistent with field observations of "tree wells" (Faria et al. 2000; Sturm 1992) with less snow immediately adjacent to the trunk, a combined result of high rates of canopy interception and ablation. The localized snowmelt energy contribution from warm trunks may have limited watershed-scale hydrological impact but important ecological significance. For example, holes in the snow cover around plant stems and branches have been shown to facilitate the first seasonal meltwater flux and subsequent preferential meltwater transport to plant roots (Qin et al. 2013). While not evaluated here, it is possible

that daytime trunk heating could introduce the first meltwater of the season to roots at times when air and canopy temperatures remain at or below freezing. Thus, while highly localized, longwave energy from trunks may critically shape snowmelt patterns known to affect meltwater partitioning between evapotranspiration and runoff (Molotch et al. 2009) and the timing of soil water availability (Harpold et al. 2015). Furthermore, enriched ion concentrations of the near-tree snowpack (Pomeroy et al. 1999) implies that preferential melt of this snow may be important for tree geochemical loading and nutrient availability.

The thermal contribution of energy from the individual tree evaluated here extended to a distance of approximately half the tree height (Fig. 11) and exhibited strong aspect-derived anisotropy. The results could have implications beyond the snow-covered period. For example, numerous processes that are sensitive to microsite moisture and energy availability include soil moisture and tree regeneration processes such as seedling establishment (Gray and Spies 1996).

6. Conclusions

The heterogeneous heating of tree trunks and canopy elements contributes to snow surface longwave irradiance. A measurement and modeling study helped to evaluate how tree temperatures vary with solar exposure and the how the resulting longwave radiation determines spatial patterns of melt surrounding a single tree. Physically based trunk and canopy temperature models with a new radiative transfer model permitted mapping the snowmelt energy contribution from an individual tree located on a sun-exposed edge of a forest clearing.

Two trunk temperature models were evaluated: a PDE-based heat transfer model and a computationally efficient EB model including a parameterization of internal heat storage. The models simulated trunk surface temperatures on eight azimuthal trunk sides. Compared to measurements, both models performed favorably (RMSE and biases better than 1.7° and ±0.4°C), with the PDE model that simulated a bark layer best capturing daytime temperature spikes. Simulated daily maximum trunk temperatures exceeded air temperature values by 1.5°–15°C, with the highest values occurring later in the day on the southwestern side and the lowest values occurring on the shaded, northern side of the trunk. Measurements and models agreed that trunk surfaces returned to or cooled below ambient air temperature values near sunset; however, the PDE model tracked internal heat storage from daytime surface heating well into the night. Canopy needle temperatures modeled with the EB approach were within the range of thermocouple measurements and

exceeded daytime air temperatures by as much as 5.5°C depending on solar exposure.

The radiative transfer model estimated that trees provided substantial longwave irradiance to a distance of approximately half the tree height, with higher values on the southern sides of the sun-exposed tree. Assuming that a tree radiates longwave energy at the air temperature resulted in snowmelt errors of 2–3 mm day^{-1} during the study period, highlighting the importance of computing the vegetation EB in snow model simulations. Trunks had highly localized and relatively low longwave energy influence on snowmelt compared to that of the canopy, suggesting that snow hydrology models need not explicitly resolve trunk temperatures. Despite the limited influence of trunk longwave irradiance on snowmelt, localized melt around individual trunks may be of great ecohydrological and biogeochemical importance because of induction of preferential melt and the high geochemical loading to snow near tree trunks. Overall, the temperature and radiative transfer models presented here offer critical inroads to 1) develop scaling relationships for improved representation of tree temperature distributions and subcanopy snow-cover depletion within land surface model schemes and 2) improve understanding of plot-scale meltwater production and the pathways by which snowmelt becomes available for uptake by tree roots.

APPENDIX

View Factor Calculations

The analytical view factor analysis presented by Holchendler and Laverty (1974) solves the single integral over the finite area of the (tree) element A_i:

$$F_{dS_j \to A_i} = \frac{1}{\pi} \int_{A_i} \frac{\cos\theta_j \cos\theta_i}{R^2} dA_i. \qquad (A1)$$

To compute the full view factor [i.e., Eq. (15)], Eq. (A1) requires an additional integration over the snow surface area of interest (i.e., grid cell). Also note that Eq. (A1) solves for the reciprocal of F needed to estimate the longwave contribution from a tree element to the snow surface. The reciprocity relation requires that $A_i F_{i \to j} = A_j F_{j \to i}$, where A_i and A_j are the areas of two (finite) surfaces of interest (Howell et al. 2010). Thus, knowledge of the two surface areas and F from the perspective of one surface can be used to estimate F for the other surface.

The canopy and trunk were modeled as a full and truncated cone with a canopy radius r_c, trunk radii of $r_{tr,1}$ (at canopy base height) and $r_{tr,2}$ (at ground level), and heights of h_c and h_{tr}, respectively (Fig. 4). The minimum trunk radius at the height of the canopy base was estimated assuming a linear trunk taper with height from the ground level. The general analytical expression for the view factor $F_{dS_j \to tc}$ for an unobstructed upright truncated cone of height h and minimum and maximum radii r_1 and r_2 relative to a differential horizontal surface dS_j at distance d from the central axis is

$$F_{dS \to tc} = \frac{1}{\pi} \left\{ \tan^{-1}\left(\sqrt{\frac{X+1}{X-1}} \right) + \frac{Z-1}{\sqrt{(Z-1)^2 + h^2}} \tan^{-1}\left[\sqrt{\frac{(Z-1)^2 + h^2}{X^2 - 1}} \right] \right.$$
$$\left. - \frac{(X^2 - Z^2 + h^2)}{\sqrt{BA}} \tan^{-1}\left[\sqrt{\frac{A(X-1)}{B(X+1)}} \right] \right\}, \qquad (A2)$$

where $X = d/r_2$, $Z = r_1/r_2$, $A = (X + Z)^2 + h^2$, and $B = (X - Z)^2 + h^2$ (Holchendler and Laverty 1974; Howell et al. 2010).

Equation (A2) was used to estimate F of a full conical canopy shape by setting the minimum canopy

radius r_1 to 0.001 m. Thus, the canopy crown view factor F_c was estimated as the difference between view factors for a complete cone and a lower truncated cone with respective heights of h_c and h_{tr}: $F_c = F_{C2} - F_{C3}$ (see Fig. 4) via the principle of superposition. To estimate

the canopy-contributed longwave irradiance to the snow surface including that directly beneath the canopy, the view factor of the underside of the conical canopy model F_{uc} excluding that obstructed by the conical trunk was computed (see Fig. 4). Holchendler and Laverty (1974) provide a closed-form solution for computing F from a horizontal differential surface element dS_j to the underside of an annular disk bisected and partially obstructed by a vertical cone:

$$F_{dS \to uc} = \frac{1}{2\pi}\cos^{-1}\left(\frac{r_{tr,1}}{r_c}\right) + \frac{d^2 - r_{tr,1}^2 + h_{cb}^2}{\pi\sqrt{A_1 B_1}}\tan^{-1}\left[\sqrt{\frac{A_1(d - r_{tr,2})}{B_1(d + r_{tr,2})}}\right] - \frac{d^2 - r_c^2 + h^2}{\pi\sqrt{A_3 B_3}}\tan^{-1}\left[\sqrt{\frac{A_3(dr_c - r_{tr,2}r_{tr,1} + C)}{B_3(dr_c + r_{tr,2}r_{tr,1} - C)}}\right],$$

(A3)

where $A_n = (d + r_n)^2 + h_{cb}^2$, $B_n = (d - r_n)^2 + h_{cb}^2$, $C = \sqrt{(d^2 - r_2^2)(r_3^2 - r_1^2)}$, and $D = \sqrt{(r_1 - r_2)^2 + h_{cb}^2}$. Equations (A2) and (A3) were integrated numerically in MATLAB to estimate F for a finite snow surface area of an L-length (m) rectilinear grid cell using the equation:

$$F_{S \to A_i} = \frac{1}{L}\int_d^{d+L} F_{dS \to A_i}\, dR.$$

(A4)

REFERENCES

Allen, R. G., R. Trezza, and M. Tasumi, 2006: Analytical integrated functions for daily solar radiation on slopes. *Agric. For. Meteor.*, **139**, 55–73, doi:10.1016/j.agrformet.2006.05.012.

Bales, R. C., N. P. Molotch, T. H. Painter, M. D. Dettinger, R. Rice, and J. Dozier, 2006: Mountain hydrology of the western United States. *Water Resour. Res.*, **42**, W08432, doi:10.1029/2005WR004387.

Bernier, P. Y., and R. Swanson, 1993: The influence of opening size on snow evaporation in the forests of the Alberta Foothills. *Can. J. For. Res.*, **23**, 239–244, doi:10.1139/x93-032.

Boudreault, L.-É., A. Bechmann, L. Tarvainen, L. Klemedtsson, I. Shendryk, and E. Dellwik, 2015: A LiDAR method of canopy structure retrieval for wind modeling of heterogeneous forests. *Agric. For. Meteor.*, **201**, 86–97, doi:10.1016/j.agrformet.2014.10.014.

Braud, I., 2000: SiSPAT, a numerical model of water and energy fluxes in the soil–plant–atmosphere continuum. Version 3.0, SiSPAT User's Manual, 107 pp.

Burles, K., and S. Boon, 2011: Snowmelt energy balance in a burned forest plot, Crowsnest Pass, Alberta, Canada. *Hydrol. Processes*, **25**, 3012–3029, doi:10.1002/hyp.8067.

Coops, N. C., S. N. Gillanders, M. A. Wulder, S. E. Gergel, T. Nelson, and N. R. Goodwin, 2010: Assessing changes in forest fragmentation following infestation using time series Landsat imagery. *For. Ecol. Manage.*, **259**, 2355–2365, doi:10.1016/j.foreco.2010.03.008.

Denny, M. W., 1993: *Air and Water: The Biology and Physics of Life's Media.* Princeton University Press, 360 pp.

Derby, R. W., and D. M. Gates, 1966: The temperature of tree trunks—Calculated and observed. *Amer. J. Bot.*, **53**, 580–587, doi:10.2307/2440008.

Duffie, J. A., and W. A. Beckman, 1980: *Solar Engineering of Thermal Processes.* Wiley, 762 pp.

Ellis, C., J. Pomeroy, and T. Link, 2013: Modeling increases in snowmelt yield and desynchronization resulting from forest gap-thinning treatments in a northern mountain headwater basin. *Water Resour. Res.*, **49**, 936–949, doi:10.1002/wrcr.20089.

Essery, R., and Coauthors, 2008: Radiative transfer modeling of a coniferous canopy characterized by airborne remote sensing. *J. Hydrometeor.*, **9**, 228–241, doi:10.1175/2007JHM870.1.

Faria, D. A., J. W. Pomeroy, and R. L. H. Essery, 2000: Effect of covariance between ablation and snow water equivalent on depletion of snow-covered area in a forest. *Hydrol. Processes*, **14**, 2683–2695, doi:10.1002/1099-1085(20001030)14:15<2683::AID-HYP86>3.0.CO;2-N.

Garnier, B. J., and A. Ohmura, 1968: A method for calculating direct shortwave radiation income of slopes. *J. Appl. Meteor.*, **7**, 796–800, doi:10.1175/1520-0450(1968)007<0796:AMOCTD>2.0.CO;2.

Gelfan, A., J. Pomeroy, and L. Kuchment, 2004: Modeling forest cover influences on snow accumulation, sublimation, and melt. *J. Hydrometeor.*, **5**, 785–803, doi:10.1175/1525-7541(2004)005<0785:MFCIOS>2.0.CO;2.

Giesbrecht, M. A., and M. K. Woo, 2000: Simulation of snowmelt in a subarctic spruce woodland: 2. Open woodland model. *Water Resour. Res.*, **36**, 2287–2295, doi:10.1029/2000WR900093.

Gouttevin, I., M. Lehning, T. Jonas, D. Gustafsson, and M. Mölder, 2015: A two-layer canopy model with thermal inertia for an improved snowpack energy balance below needleleaf forest (model SNOWPACK, version 3.2. 1, revision 741). *Geosci. Model Dev.*, **8**, 2379–2398, doi:10.5194/gmd-8-2379-2015.

Gray, A. N., and T. A. Spies, 1996: Gap size, within-gap position and canopy structure effects on conifer seedling establishment. *J. Ecol.*, **84**, 635–645, doi:10.2307/2261327.

Hall, R., D. Davidson, and D. Peddle, 2003: Ground and remote estimation of leaf area index in Rocky Mountain forest stands, Kananaskis, Alberta. *Can. J. Rem. Sens.*, **29**, 411–427, doi:10.5589/m03-012.

Harpold, A. A., N. P. Molotch, K. N. Musselman, R. C. Bales, P. B. Kirchner, M. Litvak, and P. D. Brooks, 2015: Soil moisture response to snowmelt timing in mixed-conifer subalpine forests. *Hydrol. Processes*, **29**, 2782–2798, doi:10.1002/hyp.10400.

Haughton, N., and Coauthors, 2016: The plumbing of land surface models: Is poor performance a result of methodology or data quality? *J. Hydrometeor.*, **17**, 1705–1723, doi:10.1175/JHM-D-15-0171.1.

Haverd, V., M. Cuntz, R. Leuning, and H. Keith, 2007: Air and biomass heat storage fluxes in a forest canopy: Calculation within a soil vegetation atmosphere transfer model. *Agric. For. Meteor.*, **147**, 125–139, doi:10.1016/j.agrformet.2007.07.006.

Högström, U., 1996: Review of some basic characteristics of the atmospheric surface layer. *Bound.-Layer Meteor.*, **78**, 215–246, doi:10.1007/BF00120937.

Holchendler, J., and W. Laverty, 1974: Configuration factors for radiant heat exchange in cavities bounded at the ends by parallel disks and having conical center bodies. *J. Heat Transfer*, **96**, 254–257, doi:10.1115/1.3450177.

Howell, J. R., R. Siegel, and M. P. Menguc, 2010: *Thermal Radiation Heat Transfer.* CRC Press, 987 pp.

Kain, G., M. C. Barbu, S. Hinterreiter, K. Richter, and A. Petutschnigg, 2013: Using bark as a heat insulation material. *BioResources*, **8**, 3718–3731, doi:10.15376/biores.8.3.3718-3731.

Koivusalo, H., and T. Kokkonen, 2002: Snow processes in a forest clearing and in a coniferous forest. *J. Hydrol.*, **262**, 145–164, doi:10.1016/S0022-1694(02)00031-8.

Lawler, R. R., and T. E. Link, 2011: Quantification of incoming all-wave radiation in discontinuous forest canopies with application to snowmelt prediction. *Hydrol. Processes*, **25**, 3322–3331, doi:10.1002/hyp.8150.

Levia, D. F., and E. E. Frost, 2003: A review and evaluation of stemflow literature in the hydrologic and biogeochemical cycles of forested and agricultural ecosystems. *J. Hydrol.*, **274**, 1–29, doi:10.1016/S0022-1694(02)00399-2.

Link, T. E., and D. Marks, 1999: Point simulation of seasonal snow cover dynamics beneath boreal forest canopies. *J. Geophys. Res.*, **104**, 27 841–27 857, doi:10.1029/1998JD200121.

Lundquist, J. D., S. E. Dickerson-Lange, J. A. Lutz, and N. C. Cristea, 2013: Lower forest density enhances snow retention in regions with warmer winters: A global framework developed from plot-scale observations and modeling. *Water Resour. Res.*, **49**, 6356–6370, doi:10.1002/wrcr.20504.

Moeser, D., F. Morsdorf, and T. Jonas, 2015: Novel forest structure metrics from airborne LiDAR data for improved snow interception estimation. *Agric. For. Meteor.*, **208**, 40–49, doi:10.1016/j.agrformet.2015.04.013.

Molotch, N. P., P. D. Brooks, S. P. Burns, M. Litvak, R. K. Monson, J. R. McConnell, and K. Musselman, 2009: Eco-hydrological controls on snowmelt partitioning in mixed-conifer sub-alpine forests. *Ecohydrology*, **2**, 129–142, doi:10.1002/eco.48.

Monson, R. K., and Coauthors, 2005: Climatic influences on net ecosystem CO_2 exchange during the transition from wintertime carbon source to springtime carbon sink in a high-elevation, subalpine forest. *Oecologia*, **146**, 130–147, doi:10.1007/s00442-005-0169-2.

Monteith, J., and M. Unsworth, 2013: *Principles of Environmental Physics: Plants, Animals, and the Atmosphere.* 4th ed., Academic Press, 422 pp.

Musselman, K. N., N. P. Molotch, and P. D. Brooks, 2008: Effects of vegetation on snow accumulation and ablation in a mid-latitude sub-alpine forest. *Hydrol. Processes*, **22**, 2767–2776, doi:10.1002/hyp.7050.

——, ——, S. A. Margulis, P. Kirchner, and R. C. Bales, 2012: Influence of canopy structure and direct beam solar irradiance on snowmelt rates in a mixed conifer forest. *Agric. For. Meteor.*, **161**, 46–56, doi:10.1016/j.agrformet.2012.03.011.

——, S. A. Margulis, and N. P. Molotch, 2013: Estimation of solar direct beam transmittance of conifer canopies from airborne LiDAR. *Remote Sens. Environ.*, **136**, 402–415, doi:10.1016/j.rse.2013.05.021.

——, J. W. Pomeroy, and T. E. Link, 2015: Variability in shortwave irradiance caused by forest gaps: Measurements, modelling, and implications for snow energetics. *Agric. For. Meteor.*, **207**, 69–82, doi:10.1016/j.agrformet.2015.03.014.

Parviainen, J., and J. Pomeroy, 2000: Multiple-scale modelling of forest snow sublimation: Initial findings. *Hydrol. Processes*, **14**, 2669–2681, doi:10.1002/1099-1085(20001030)14:15<2669::AID-HYP85>3.0.CO;2-Q.

Pomeroy, J. W., and R. Granger, 1997: Sustainability of the western Canadian boreal forest under changing hydrological conditions. I. Snow accumulation and ablation. *IAHS Publ.*, **240**, 237–242.

——, J. Parviainen, N. Hedstrom, and D. M. Gray, 1998: Coupled modelling of forest snow interception and sublimation. *Hydrol. Processes*, **12**, 2317–2337, doi:10.1002/(SICI)1099-1085(199812)12:15<2317::AID-HYP799>3.0.CO;2-X.

——, T. Davies, H. Jones, P. Marsh, N. Peters, and M. Tranter, 1999: Transformations of snow chemistry in the boreal forest: Accumulation and volatilization. *Hydrol. Processes*, **13**, 2257–2273, doi:10.1002/(SICI)1099-1085(199910)13:14/15<2257::AID-HYP874>3.0.CO;2-G.

——, C. Ellis, A. Rowlands, R. Essery, J. Hardy, T. Link, D. Marks, and J. E. Sicart, 2008: Spatial variability of shortwave irradiance for snowmelt in forests. *J. Hydrometeor.*, **9**, 1482–1490, doi:10.1175/2008JHM867.1.

——, D. Marks, T. Link, C. Ellis, J. Hardy, A. Rowlands, and R. Granger, 2009: The impact of coniferous forest temperature on incoming longwave radiation to melting snow. *Hydrol. Processes*, **23**, 2513–2525, doi:10.1002/hyp.7325.

Qin, Y., X. Chen, K. Zhou, P. Klenk, K. Roth, and L. Sun, 2013: Ground-penetrating radar for monitoring the distribution of near-surface soil water content in the Gurbantünggüt Desert. *Environ. Earth Sci.*, **70**, 2883–2893, doi:10.1007/s12665-013-2528-3.

Riitters, K., J. Wickham, R. O'Neill, B. Jones, and E. Smith, 2000: Global-scale patterns of forest fragmentation. *Conserv. Ecol.*, **4**, 3, doi:10.5751/ES-00209-040203.

Seyednasrollah, B., and M. Kumar, 2014: Net radiation in a snow-covered discontinuous forest gap for a range of gap sizes and topographic configurations. *J. Geophys. Res. Atmos.*, **119**, 10 323–10 342, doi:10.1002/2014JD021809.

——, ——, and T. E. Link, 2013: On the role of vegetation density on net snow cover radiation at the forest floor. *J. Geophys. Res. Atmos.*, **118**, 8359–8374, doi:10.1002/jgrd.50575.

Sicart, J. E., R. L. H. Essery, J. W. Pomeroy, J. Hardy, T. Link, and D. Marks, 2004: A sensitivity study of daytime net radiation during snowmelt to forest canopy and atmospheric conditions. *J. Hydrometeor.*, **5**, 774–784, doi:10.1175/1525-7541(2004)005<0774:ASSODN>2.0.CO;2.

Sturm, M., 1992: Snow distribution and heat flow in the taiga. *Arct. Alp. Res.*, **24**, 145–152, doi:10.2307/1551534.

Trujillo, E., N. P. Molotch, M. L. Goulden, A. E. Kelly, and R. C. Bales, 2012: Elevation-dependent influence of snow accumulation on forest greening. *Nat. Geosci.*, **5**, 705–709, doi:10.1038/ngeo1571.

Vidale, P. L., D. Lüthi, C. Frei, S. I. Seneviratne, and C. Schär, 2003: Predictability and uncertainty in a regional climate model. *J. Geophys. Res.*, **108**, 4586, doi:10.1029/2002JD002810.

Webster, C., N. Rutter, F. Zahner, and T. Jonas, 2016: Modeling subcanopy incoming longwave radiation to seasonal snow using air and tree trunk temperatures. *J. Geophys. Res. Atmos.*, **121**, 1220–1235, doi:10.1002/2015JD024099.

Woo, M. K., and M. A. Giesbrecht, 2000: Simulation of snowmelt in a subarctic spruce woodland: 1. Tree model. *Water Resour. Res.*, **36**, 2275–2285, doi:10.1029/2000WR900094.